

## ELECTRON DISTRIBUTION FUNCTIONS IN SOLAR FLARES FROM COMBINED X-RAY AND EXTREME-ULTRAVIOLET OBSERVATIONS

M. BATTAGLIA<sup>1</sup> AND E. P. KONTAR<sup>2</sup>

<sup>1</sup> Institute of 4D Technologies, School of Engineering, University of Applied Sciences and Arts Northwestern Switzerland, 5210 Windisch, Switzerland; [marina.battaglia@fhnw.ch](mailto:marina.battaglia@fhnw.ch)

<sup>2</sup> SUPA, School of Physics and Astronomy, University of Glasgow, G12 8QQ, UK  
Received 2013 July 11; accepted 2013 October 14; published 2013 November 27

### ABSTRACT

Simultaneous solar flare observations with *SDO* and *RHESSI* provide spatially resolved information about hot plasma and energetic particles in flares. *RHESSI* allows the properties of both hot ( $\gtrsim 8$  MK) thermal plasma and non-thermal electron distributions to be inferred, while *SDO/AIA* is more sensitive to lower temperatures. We present and implement a new method to reconstruct electron distribution functions from *SDO/AIA* data. The combined analysis of *RHESSI* and *AIA* data allows the electron distribution function to be inferred over the broad energy range from 0.1 keV up to a few tens of keV. The analysis of two well-observed flares suggests that the distributions in general agree to within a factor of three when the *RHESSI* values are extrapolated into the intermediate range 1–3 keV, with *AIA* systematically predicting lower electron fluxes. Possible instrumental and numerical effects, as well as potential physical origins for this discrepancy, are discussed. The inferred electron distribution functions in general show one or two nearly Maxwellian components at energies below  $\sim 15$  keV and a non-thermal tail above.

*Key words:* Sun: chromosphere – Sun: flares – Sun: X-rays, gamma rays

*Online-only material:* color figures

### 1. INTRODUCTION

Solar flares accelerate large numbers of particles within seconds and maintain efficient acceleration over timescales of minutes to tens of minutes. Hard X-ray (HXR) observations of solar flares provide information on the electron acceleration and transport in solar flares and are crucial to better constrain various flare models (e.g., Holman et al. 2011, as a recent review). Observations with *RHESSI* (Lin et al. 2002) have significantly enriched our understanding of solar flare physics by providing accurate spatially resolved soft X-ray (SXR) and HXR spectra, which are used as the input to deduce the properties of the accelerated electrons (e.g., Kontar et al. 2011, as a recent review). *RHESSI* also makes it possible to analyze individual source spectra (coronal sources, footpoints), by means of imaging spectroscopy (e.g., Emslie et al. 2003; Battaglia & Benz 2006). The technique was recently used by Simões & Kontar (2013) to infer the characteristic electron acceleration rates at the looptop and at the footpoints of a number of flares, finding strong indication for particle trapping at the top of flaring loops. However, *RHESSI* detectors only provide X-ray observations above 3 keV, or even higher energies during large flares when attenuators are placed in front of the detectors to reduce dead-time, which results in much reduced flux at energies below  $\sim 6$ – $12$  keV (Smith et al. 2002). While priceless to infer the properties of deka-keV electrons, it leaves an observational gap for electrons below 3 keV. Due to the typical shape of flare spectra, particles at these energies constitute the larger part of the total particle number in flares. It is important to extend the diagnostics to energies below 3 keV to answer questions such as whether the distribution at these energies is an iso-thermal Maxwellian. Unlike the higher X-ray energies, hot flaring plasma is normally studied using EUV and X-ray line emissions. Observations of the line intensities provide information on the temperature distribution of the solar plasma.

With the recent launch of the Atmospheric Imaging Assembly (*AIA*) on board the *Solar Dynamics Observatory* (*SDO*; Lemen et al. 2012), it is now possible to deduce differential emission measures (DEMs) over a broad range of coronal temperatures with high spatial resolution. Complementing SXR and HXR observations with EUV observations allows the mean electron flux spectrum to be deduced over a wide range of energies from as low as 0.1 keV up to tens of keV.

In this paper we develop a method to infer the low-energy part of the electron flux spectrum from DEMs and apply the method to spatially resolved *AIA* observations. We first demonstrate the method on a set of synthetic DEMs for which the electron distribution function is known and then apply it to flare observations. Using simultaneous X-ray and EUV observations, we deduce, for the first time, the mean electron flux spectrum and estimate the local electron distribution function in various regions of the flaring atmosphere. The observations show that locally non-thermal electrons constitute a relatively modest fraction of the order of  $10^{-2}$  of the total electron numbers. Different flaring regions demonstrate distinct electron distributions: footpoint regions can be viewed consistent with a Maxwellian distribution and a non-thermal tail, while an above-the-looptop source deviates from a Maxwellian in the range above 0.5 keV.

### 2. RECONSTRUCTION OF ELECTRON DISTRIBUTION FUNCTION FROM DEM( $T$ )

Using line observations, the properties of thermal plasma are traditionally characterized by the DEM  $\xi(T)$  ( $\text{cm}^{-3} \text{K}^{-1}$ ). Assuming a locally Maxwellian distribution with local temperature  $T(r)$  and density  $n(r)$  at spatial coordinate  $r$ ,  $\xi(T)$  characterizes the amount of plasma at various plasma temperatures  $T(r)$ , so that the integral over  $T$  gives the total EM  $\text{EM} = \int \xi(T) dT$ . The Maxwellian

distribution at temperature  $T(r)$  is given as

$$F(E, r) = \frac{2^{3/2}}{(\pi m_e)^{1/2}} \frac{n(r)E}{(k_B T(r))^{3/2}} \exp(-E/k_B T(r)), \quad (1)$$

where  $E$  is the electron kinetic energy,  $m_e$  is the electron mass, and  $k_b$  is the Boltzmann constant. This is related to the mean electron flux spectrum  $\langle nVF \rangle$  in the emitting volume  $V$  and the DEM  $\xi(T)$  following, e.g., Brown & Emslie (1988):

$$\langle nVF \rangle = \int_V n(r)F(E, r) dV \quad (2)$$

$$= \int_T n(r) \frac{2^{3/2}}{(\pi m_e)^{1/2}} \frac{n(r)E}{(k_B T(r))^{3/2}} \exp(-E/k_B T(r)) \frac{dV}{dT} dT, \quad (3)$$

where  $n^2 dV/dT = \xi(T)$  is the DEM and thus

$$\langle nVF \rangle = \frac{2^{3/2} E}{(\pi m_e)^{1/2}} \int_0^\infty \frac{\xi(T)}{(k_B T)^{3/2}} \exp(-E/k_B T) dT. \quad (4)$$

Therefore, knowing the DEM, one can compute the electron flux spectrum in the emitting volume (electrons  $\text{keV}^{-1} \text{s}^{-1} \text{cm}^{-2}$ ). Although Equation (4), which is an equivalent of the Laplace transform of a function  $f(t)$

$$F(s) = \int_0^\infty \exp(-st) f(t) dt, \quad (5)$$

is formally a straightforward integration over temperature, the numerical integration could be rather challenging due to the exponential kernel (e.g., Prato et al. 2006). Following Rossberg (2008), we rewrite the Laplace transform (Equation (5)) via the convolution integral, which will allow efficient numerical computations of  $\langle nVF \rangle$  via  $\xi(T)$  and vice versa. Using the change of variables  $s = \exp(y)$  and  $t = \exp(-x)$ , let us rewrite Equation (5) in the following form:

$$F(e^y) = \int_{-\infty}^\infty K(y-x) h(x) dx, \quad (6)$$

where  $K(y-x) = \exp(y-x) \exp[-\exp(y-x)]$  and  $h(x) = \phi(e^{-x})$  with  $\phi(t) = \int_0^t f(t') dt'$ . Equation (4) can be similarly brought into the form of Equation (5) using the variable change

$$t = 1/T; \quad \frac{dt}{dT} = -\frac{1}{T^2}; \quad dT = -\frac{1}{t^2} dt, \quad (7)$$

which results in

$$\langle nVF \rangle = \frac{2^{3/2} E}{(\pi m_e)^{1/2} 2k_B^{3/2}} \int_0^\infty \frac{\xi(T(t))}{t^{1/2}} \exp(-Et/k_B) dt, \quad (8)$$

so that  $f(t) = (\xi(T(t))/t^{1/2})$  and  $\exp(-st) = \exp(-Et/k_B)$  in Equation (5), which is then brought into the form of Equation (6) and solved.

### 2.1. Application on Synthetic DEM

We illustrate the method using two synthetic DEMs. The first is a single-temperature DEM, i.e., a  $\delta$ -function in temperature space (Figure 1, top) at temperature  $T_0 = 5$  MK. The mean electron flux spectrum corresponding to this DEM is calculated

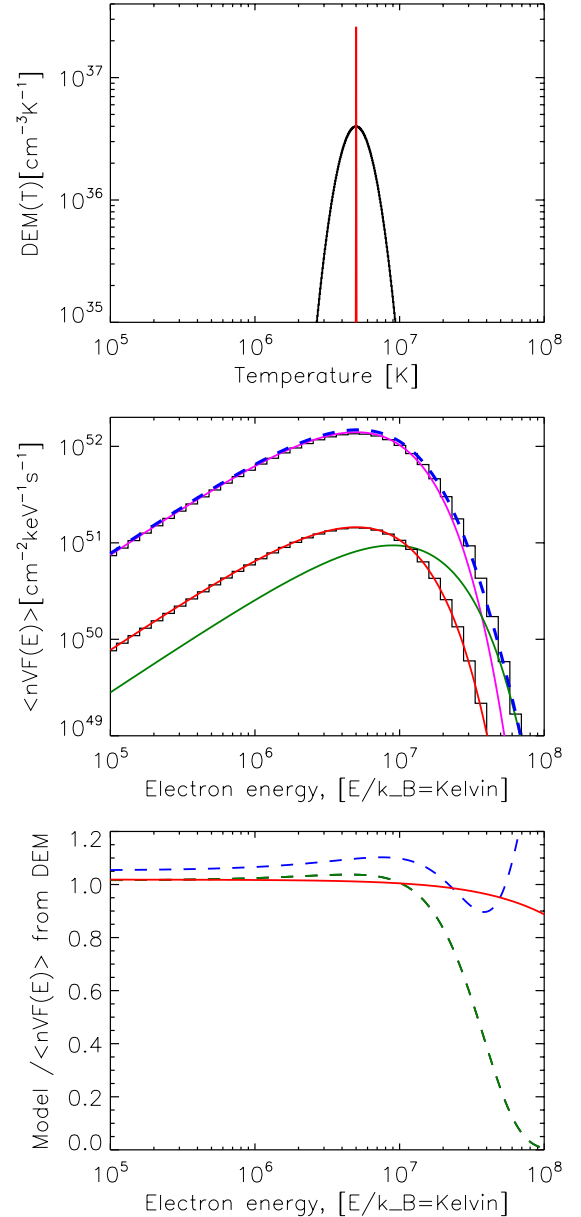


**Figure 1.** Top: synthetic DEM ( $\text{cm}^{-3} \text{K}^{-1}$ ) as a function of  $T$  for peak temperature 5 MK and two different widths (red:  $\delta$ -function, black:  $\sigma = 0.1$ , compare Equation (10)). Middle: reconstructed mean electron flux spectrum from DEM (black lines). The total EM of the DEM with width  $\sigma = 0.1$  was chosen one order of magnitude larger than the  $\delta$ -function to give clearly distinguishable electron spectra. The red line gives a Maxwellian distribution at temperature 5 MK. The purple and green lines are Maxwellian distributions at 5 MK and 9 MK; the dashed blue line is the sum of these two Maxwellians. Bottom: model flux divided by flux from DEM in the case of a  $\delta$ -function DEM (red solid line), and in the case of DEM of width  $\sigma = 0.1$  relative to a single-temperature Maxwellian (dashed green) and two Maxwellians at 5 MK and 9 MK (dashed blue line).

(A color version of this figure is available in the online journal.)

using Equations (4)–(8). The result is shown in the middle panel of Figure 1. This is compared to the Maxwellian distribution as defined in Equation (1). From Equation (2) one finds the mean electron flux spectrum for a uniform distribution over the whole volume as

$$\langle nVF \rangle = n_e^2 V \left( \frac{2}{k_B T} \right)^{3/2} \frac{E}{(\pi m_e)^{1/2}} \exp(-E/k_B T), \quad (9)$$

where  $n_e^2 V = \text{EM}$  is the total emission EM. As Figure 1 indicates, there is a very close agreement (better than 2% except for temperatures above  $\sim 2 \times 10^7$  K, where numerical effects become noticeable) between the analytical solution (Equation (9)) and the mean electron flux spectrum found by integrating the DEM (Equation (8)), validating the method. The second synthetic DEM for which the method is demonstrated is a Gaussian DEM function in  $\log T$ :

$$\xi(T) = \frac{\xi_0}{\sqrt{2\pi}\sigma^2} \exp(-(\log T - \log T_0)^2 / (2\sigma^2)), \quad (10)$$

with a peak temperature of  $T_0 = 5$  MK, width  $\sigma = 0.1$ , and  $\xi_0 = 10^{36} \text{ cm}^{-3} \text{ K}^{-1}$ , where  $\xi_0$  was chosen such that the total EM is one order of magnitude larger than in the first case to simplify the presentation in Figure 1. We define the total EM as

$$\text{EM} = \int_{T_{\min}}^{T_{\max}} \xi(T) dT, \quad (11)$$

where  $T_{\min} = 0.01$  MK and  $T_{\max} = 100$  MK in the synthetic case. We again compare the electron flux spectrum inferred from the DEM with a single-temperature Maxwellian. Since a Gaussian DEM function does not represent a single-temperature distribution, some discrepancy, especially at higher energies, can be expected. As Figure 1 demonstrates, the inferred mean electron flux spectrum is still in good agreement with the single-temperature model at low energies, but diverges at higher energies, due to the contribution of non-zero DEM at temperatures higher than the peak temperature that was used for the Maxwellian model. This interpretation is supported by the fact that adding an additional Maxwellian temperature model with temperature 9 MK and emission measure 0.09 times the total EM of the first DEM model adequately describes the high-energy component and leads to a better agreement except for the highest temperatures (see Figure 1, blue dashed lines).

### 3. DISTRIBUTION FUNCTIONS FROM *RHESSI* AND *SDO/AIA* OBSERVATIONS

We now apply the method to two events for which there were good simultaneous *RHESSI* and *AIA* observations. The first event was a *GOES* class C4.1 event on 2010 August 14 (henceforth SOL2010-08-14T10:05) with HXR peak time around 09:46 UT. It displays an EUV loop that is co-spatial with an SXR loop seen in *RHESSI* images. Because the event was relatively weak, the regions of interest were not saturated in all *AIA* wavelength channels (see Battaglia & Kontar 2012). The second event was a *GOES* M7.7 limb event on 2012 July 19 (henceforth SOL2012-07-19T05:58) with the first HXR peak at around 05:22 UT, showing two footpoints, an SXR coronal source, and an HXR above-the-looptop source. In this event the exposure times in all *AIA* wavelengths were short enough to provide unsaturated images even during the flare peak. For both events we chose the time interval with highest observed X-ray energies within the limitations given by both instruments such as saturation of *AIA* images and pileup in *RHESSI* spectra. For both events the mean electron distribution function at energies below  $\sim 1$  keV is calculated using *AIA* DEM measurements. *RHESSI* observations are used to find the distribution function above 3 keV up to the highest observed X-ray energies ( $\sim 25$  keV for SOL2010-08-14T10:05 and 80 keV for SOL2012-07-19T05:58).

#### 3.1. SOL2010-08-14T10:05

For this flare we chose a time interval during the rise phase of the flare when *AIA* images were not saturated, and a small non-thermal tail was observed with *RHESSI*. Panel (a) in Figure 2 shows a 131 Å *AIA* image overlaid with 20%, 30%, and 50% contours from a *RHESSI* 8–10 keV CLEAN image, calculated using grids 3–8 and natural weighting with clean-beam-width-factor 1.7 (corresponding to an effective beam FWHM of 9.1 arcsec). The *RHESSI* source is co-spatial with the top of the EUV loop and extending downward along the legs of the EUV loop. The bulk of the EUV emission originates from ribbons at the bottom of the loop, and *AIA* images in these regions consequently are saturated in most wavelength bands. Here we focus on the part of the loop that is co-spatial with the *RHESSI* source where no saturation occurred and the regularized inversion to find the DEM (Kontar et al. 2005) could be made with high confidence.

##### 3.1.1. *RHESSI* Spectrum and Electron Flux Distribution

The *RHESSI* full Sun spectrum suggests the presence of a thermal component and a small non-thermal tail extending to about 30 keV. The spectrum was fitted between 09:42 and 09:43 UT (attenuator state 0), during the rise phase of the flare but before pileup started to dominate energies above 10 keV (Smith et al. 2002), with a single-temperature component of 10.5 MK temperature and emission measure of  $3 \times 10^{47} \text{ cm}^{-3}$ , and a thin-target power-law component with spectral index  $\delta = 3.9$  and low-energy cutoff of 10 keV. In addition to the *RHESSI* temperature, the temperature and emission measure from *GOES* were determined for the same time interval, giving  $T_{\text{GOES}} = 9.5$  MK and  $\text{EM}_{\text{GOES}} = 5 \times 10^{47} \text{ cm}^{-3}$ . *RHESSI* images suggest that there is faint footpoint emission above  $\sim 25$  keV, but the bulk of the non-thermal emission below this energy seems to originate from the flaring loop. The mean electron flux spectrum for the thermal component is then just the Maxwellian distribution (Equation (9)). The electron flux spectrum for the non-thermal power-law component is easily found under the thin-target assumption (e.g., Tandberg-Hanssen & Emslie 1988).

##### 3.1.2. Mean Electron Flux Spectrum from *AIA* Differential Emission Measure

The *AIA* DEM per area ( $\text{cm}^{-5} \text{ K}^{-1}$ ) was calculated using the regularized inversion method developed for *RHESSI* by, e.g., Kontar et al. (2005) and adapted for *SDO/AIA* by Hannah & Kontar (2012). Such a DEM can be calculated pixel by pixel or for any finite area (e.g., Hannah & Kontar 2013; Battaglia & Kontar 2012). For direct comparison with *RHESSI* results the EUV region that is co-spatial with the *RHESSI* emission was analyzed under the assumption that the same emitting plasma is observed in all wavelengths. *RHESSI* full-Sun spectra are dominated by the flaring emission, and it is often assumed that the bulk of the emission originates from a region that corresponds to the size of the 50% contours in a *RHESSI* image. However, *AIA* images clearly outline the whole loop, as do the *RHESSI* contours down to 20%. We therefore calculate the total *AIA* DEM from several areas, namely, the ones corresponding to 50%, 30%, and 20% contours in the *RHESSI* 8–10 keV CLEAN image, and use the result from the 50% and the 20% contours as a confidence interval. The DEM from within the 50% contour is shown in panel (b) of Figure 2. The error bars represent the uncertainties of both the DEM and the temperature, i.e., the

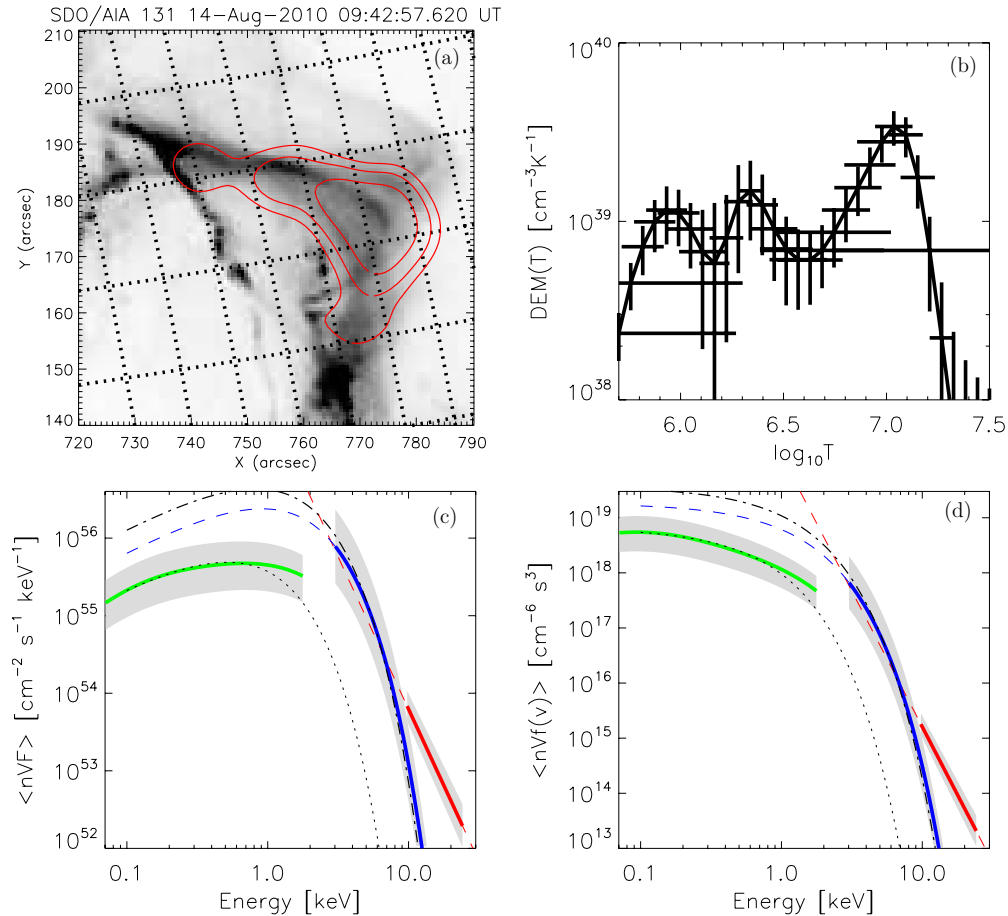


**Figure 2.** Panel (a): AIA 131 Å image overlaid with *RHESSI* contours (red; 20%, 30%, 50% in 8–10 keV CLEAN image). Panel (b): AIA DEM from area corresponding to *RHESSI* 50% contours in 8–10 keV CLEAN image. Panel (c): mean electron flux spectrum derived from AIA (green) and *RHESSI* thermal fit (blue) and non-thermal fit (red). The gray shaded area gives the confidence interval. Dashed lines indicate the extension of the flux to energies that were not observed with the respective instrument. Dash-dotted line: electron flux spectrum from *GOES* temperature and emission measure. The dotted line represents a Maxwellian distribution with  $T = 6$  MK and  $EM = 4.5 \times 10^{46} \text{ cm}^{-3}$  for illustration (not from an actual fit). Panel (d): mean electron velocity distribution.

(A color version of this figure is available in the online journal.)

effective temperature resolution, obtained from the regularized inversion (see Hannah & Kontar 2012, for full details). The DEM suggests the presence of two main temperature components, a weak one at 2 MK and one at 10 MK. The low-temperature component can most likely be attributed to background emission, while the high-temperature component is dominated by flaring emission (see also Battaglia & Kontar 2012). Note that in this case we did not impose a positivity constraint on the reconstructed DEM (see the Appendix) because the assumption of a positive DEM is quite strong and only correct in the case of purely thermal plasma. From the DEM, the mean electron flux spectrum is calculated using the method described in Section 2. Figure 2 shows the mean electron flux spectrum in units of (electrons  $\text{cm}^{-2} \text{keV}^{-1} \text{s}^{-1}$ ) as a function of energy from the combined AIA and *RHESSI* observations, where we use the result from the 50% contours and 20% contours as a confidence interval. Dividing by energy and multiplying with  $m_e^2$ , we can also display the spectrum as a velocity distribution function ( $\langle nVf(v) \rangle$ ) (Figure 2, panel (b)). The distribution found from AIA is consistent with a Maxwellian of temperature  $T = 6$  MK and emission measure  $EM = 4.5 \times 10^{46} \text{ cm}^{-3}$ , but deviates from the Maxwellian distribution at energies greater than 1 keV. The extrapolation of the *RHESSI* thermal distribution into the AIA regime is a factor  $\sim 3$  larger than the distribution from AIA. We discuss several reasons for this discrepancy in Section 4. The

overall distribution over all energies resembles particle distributions often found in the solar wind with a core-halo-strahl structure (see Marsch 2006, for a review).

### 3.2. SOL2012-07-19T05:58

For this limb event three distinct sources were observed with *RHESSI* (SXR coronal source, HXR above-the-looptop source, HXR footpoints; see Figure 3). The event has been analyzed in detail by Liu et al. (2013) with respect to several aspects of its time evolution and with a focus on the coronal densities by Krucker & Battaglia (2013). AIA exposure times were as short as 0.2 s during the course of the flare. Thus, there are unsaturated images in all wavelength channels even at the flare peak time. Here we focus on the same time interval (05:20:30 to 05:23:02 UT, attenuator state 1) used by Krucker & Battaglia (2013), who analyzed the first HXR peak using imaging spectroscopy, and we present mean electron distribution functions for three different sources observed by *RHESSI*: the SXR coronal source, the HXR above-the-looptop source, and the northern footpoint. A weak second footpoint that was likely occulted was also observed. *STEREO* images of the region suggest the presence of loops or a loop arcade for which, as seen from Earth, the southern footpoint would be occulted. Note that the northern footpoint was also likely partly occulted. Footpoint sources at higher energies are formed deeper

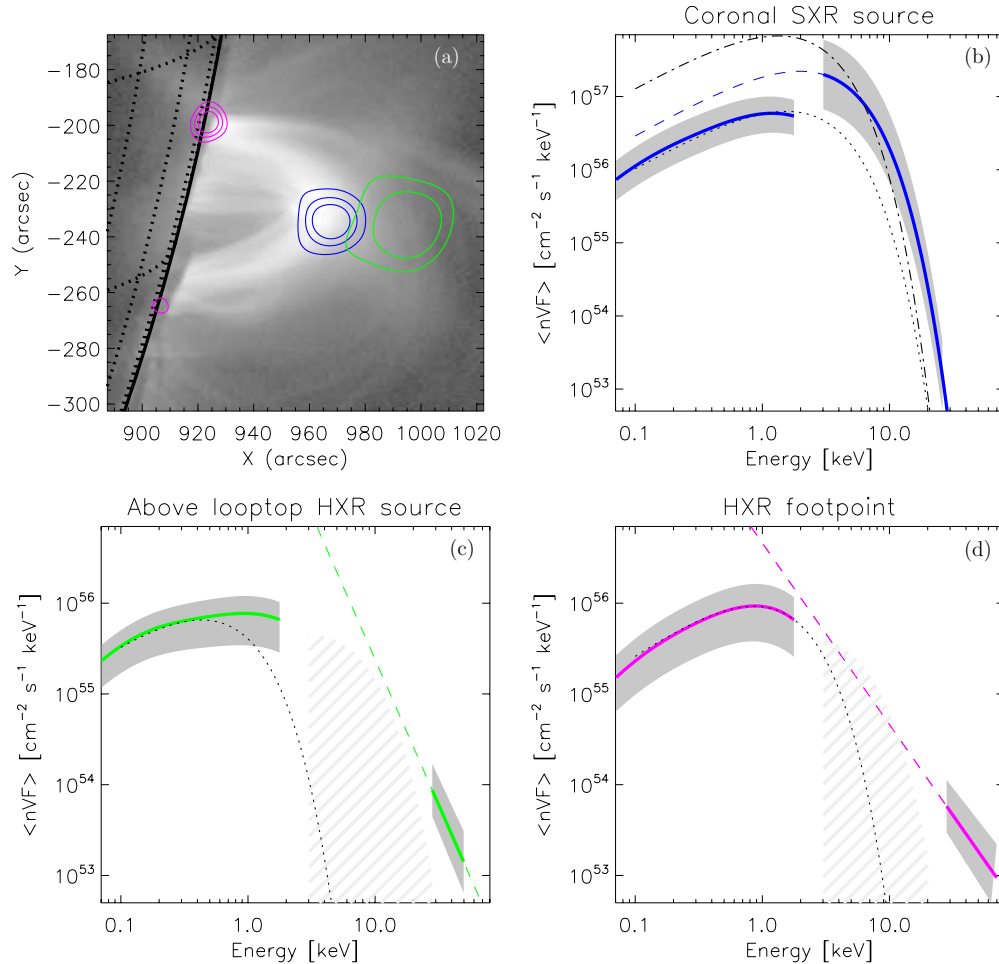


**Figure 3.** Panel (a): AIA 131 Å image of SOL2012-07-19T05:58 overlaid with *RHESSI* contours indicating the HXR footprint (purple), the coronal SXR source (blue), and the HXR above-the-looptop source (green). Panel (b): mean electron flux spectrum derived from AIA DEM measurement and *RHESSI* spectral fitting in the coronal SXR source. The dotted line indicates a Maxwellian distribution with  $T = 18$  MK and  $EM = 10^{48}$  cm $^{-3}$ . Panel (c): same as panel (b) but for the above-the-looptop source. The dotted line gives a Maxwellian with  $T = 5$  MK and  $EM = 5.5 \times 10^{46}$  cm $^{-3}$ . The upper edge of the shaded gray area at intermediate energies represents the upper limit of the flux found from a thermal fit to the reconstruction noise of the *RHESSI* image (see Section 3.2). Panel (d): same as panel (c) but for the northern footprint. The dotted line gives a Maxwellian with  $T = 10$  MK and  $EM = 10^{47}$  cm $^{-3}$  (not from an actual fit).

(A color version of this figure is available in the online journal.)

down in the chromosphere and have a vertical extent of at least 1 Mm (Battaglia & Kontar 2011; Kontar et al. 2010). Thus, the higher energies will be more occulted relative to lower energies, resulting in a softer HXR spectrum and lower observed flux. Therefore, the inferred electron flux spectrum from an occulted footprint will represent a lower limit.

### 3.2.1. *RHESSI* Spectrum and Electron Flux Distribution

Using full-Sun spectroscopy for the SXR coronal source and fitting a single-temperature thermal model, Krucker & Battaglia (2013) found  $T = 23$  MK,  $EM = 4 \times 10^{48}$  cm $^{-3}$ . The *GOES* temperature and emission measure during the corresponding time interval were  $T_{GOES} = 15.5$  MK,  $EM_{GOES} = 10^{49}$  cm $^{-3}$ . Imaging spectroscopy of the above-the-looptop HXR source resulted in an electron spectral index  $\delta = 3.2 \pm 0.2$  between 28 and 50 keV, and the spectral index of the northern footprint was  $\delta = 2.0 \pm 0.2$  between 20 and 70 keV, where a thin-target assumption was used in both cases. In the intermediate energy range between  $\sim 14$  and 20 keV the coronal source and the footprints are seen in the images. Such a complex source structure makes image reconstruction with *RHESSI* rather difficult, and it is often problematic to distinguish reconstruction noise from actual source emission (Hurford et al.

2002; Battaglia & Benz 2006). We therefore only estimated an upper limit of the electron flux in this energy range by fitting a thermal (Maxwellian) component to the X-ray spectrum (compare Figure 3).

### 3.2.2. Mean Electron Flux Spectrum from AIA Differential Emission Measure

The AIA DEM and subsequently the mean electron flux spectrum were calculated within the three regions as defined by contours from a *RHESSI* CLEAN image at 5–7 keV using grids 3, 5, 6 with uniform weighting (giving an effective CLEAN beam FWHM of 8.7 arcsec) in the case of the coronal source. For the HXR sources two-step CLEAN (Krucker et al. 2011) images at 30–70 keV were made using grids 1–5 (uniform weighting, effective beam FWHM = 3 arcsec) to image the footprints and grids 4–9 (uniform weighting, effective beam FWHM = 17 arcsec) to image the above-the-looptop source. For the HXR footprints and SXR coronal source the 30%, 50%, and 70% contours were used, and we use the 30% and 70% contours as a confidence interval. The coronal HXR source showed extended emission over a large area, and we use the 50% and 70% contours to give a confidence interval, since the 30% contours overlap with the coronal SXR source.

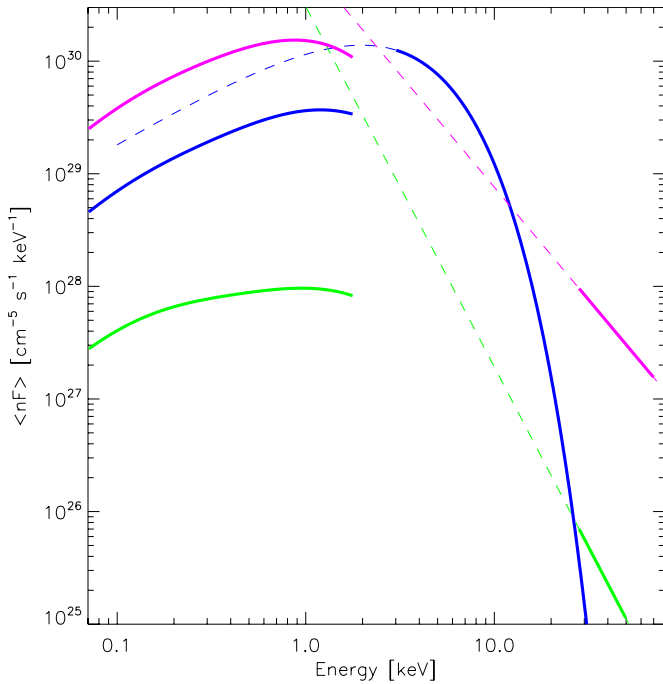


**Figure 4.** Comparison of mean electron flux spectrum *per unit volume* between the different sources of SOL2012-07-19T05:58 (compare Figure 3). Blue lines: SXR coronal source. Purple: HXR footpoints. Green: HXR above-the-looptop source.

(A color version of this figure is available in the online journal.)

We find that the mean electron flux spectrum derived from the AIA data for the coronal SXR source at energies between 0.1 and 2 keV can be approximated with a Maxwellian distribution of temperature 18 MK and emission measure  $10^{48} \text{ cm}^{-3}$ . As in the previous event, the extrapolation of the *RHESSI* spectrum to energies below 3 keV is a factor of  $\sim 2$  larger than the AIA values. The electron flux spectrum derived from AIA for the HXR footpoint is consistent with a Maxwellian at temperature  $T = 10$  MK and emission measure  $\text{EM} = 10^{47} \text{ cm}^{-3}$ . The spectrum of the HXR above-the-looptop source is consistent with a Maxwellian at temperature 5 MK and emission measure  $5.5 \times 10^{46} \text{ cm}^{-3}$  only up to about 0.6 keV and deviates from the Maxwellian distribution at higher energies. For a direct comparison of the number of electrons between the distinct regions it is useful to compare the mean electron spectra per unit volume. We define the volume as  $V = A^{3/2}$ , where  $A$  is the area of the 50% *RHESSI* contours of the SXR coronal source and the HXR above-the-looptop source. For the footpoint the effective area over which EUV emission is observed is smaller than the 50% contour by about a factor of three and the EUV emission originates from a height above the centroid of the HXR emission (Figure 3, panel (a)). Thus, we define the area of EUV emission from the footpoint region as the area of the 50% HXR contour divided by 3. Figure 4 shows a comparison between the mean electron flux spectra per unit volume from each of the sources. The figure indicates that the number of electrons per unit volume is highest in the footpoint (a factor of six larger than the SXR coronal source) and is lowest in the HXR above-the-looptop source (one order of magnitude smaller than in the SXR coronal source).

#### 4. DISCUSSION

We present and demonstrate a new method to infer the mean electron flux spectrum from DEM results derived from AIA im-

ages in different EUV wavelength channels. The method was applied to two well-observed flares. The first event displays an EUV loop that is co-spatial with an SXR loop observed by *RHESSI*, and the mean electron flux spectrum was derived for the loop as a whole. The second event can be divided into HXR footpoints, SXR coronal source, and HXR above-the-looptop source. Each of the three sources was analyzed separately. In all presented cases the result from AIA observations is a factor of 2.5–8 lower than the extrapolated thermal model from the *RHESSI* fit. There are several possible explanations for this discrepancy: the *RHESSI* fit, insensitivity of AIA to high temperatures, the method to infer the DEM, and two physically distinct particle populations. The *RHESSI* data-analysis tools are developed to a high standard, and it is believed that the instrument is well understood. In combination with good counting statistics in flares, this generally leads to rather small uncertainties of the fitted parameters (e.g., Ireland et al. 2013). However, for weak flares and when using imaging spectroscopy, it is often possible to fit different models (i.e., different temperature and emission measure) with equal  $\chi^2$  value. Further, the attenuator state affects the low-energy limit to which a confident fit can be made (Smith et al. 2002). This is not an issue for SOL2010-08-14T10:05, since no attenuator was in place, but with the thin attenuator in place during SOL2012-07-19T05:58 the spectral fit could only be performed down to 6 keV. In addition, it has recently been found that the thermal blanket thickness of the *RHESSI* instrument could be overestimated by up to 30% (B. Dennis 2013, private communication). This affects thermal fits in attenuator state 0 and in the case of SOL2010-08-14T10:05 could explain the discrepancy at least partly. All of these factors introduce an additional uncertainty not reflected in the purely statistical errors. We therefore assume an upper limit on the uncertainty of the fitted emission measure of a factor of two. This could bring the observed *RHESSI* emission measure down within the range of the AIA value. Comparison with *GOES* gives a slightly higher emission measure ( $5 \times 10^{47} \text{ cm}^{-3}$  opposed to  $3 \times 10^{47} \text{ cm}^{-3}$ ) and slightly lower temperature (9.5 MK opposed to 10.5 MK) for SOL2010-08-14T10:05. The difference is more striking for SOL2012-07-19T05:58 ( $10^{49} \text{ cm}^{-3}$  opposed to  $4 \times 10^{48} \text{ cm}^{-3}$  and 15.5 MK opposed to 23 MK). The tendency of *RHESSI* emission measures to be smaller than those derived from *GOES* observations is a common pattern observed repeatedly in the past (e.g., Hannah et al. 2008; Battaglia et al. 2005). One explanation is that this reflects *RHESSI*'s limited sensitivity to temperatures below  $\sim 8$  MK, temperatures to which *GOES* is sensitive. However, it has to be noted that *GOES* observations are full-Sun measurements with no way of knowing the exact position and extent of the source. In Figures 2 and 3 we assumed the same area as measured with *RHESSI*, but this is only an approximation. In summary, the fitted *RHESSI* emission measure in cooler flares is probably a lower limit of the true emission because of reduced sensitivity; on the other hand, the emission measure could be overestimated in the attenuator 0 state. Another explanation in certain flares is the main temperature sensitivity range of AIA. The response function of the high-temperature wavelength channels 131 Å and 193 Å peaks at 12 MK and 16 MK, respectively, and falls off sharply at higher temperatures. If the bulk of the plasma is at higher temperatures than 12–16 MK, AIA will not be sensitive to its signatures, resulting in an underestimated total emission measure. This could explain the discrepancy in the SXR coronal source of SOL2012-07-19T05:58, for which a *RHESSI* temperature of 23 MK was found. On the other hand, the *RHESSI* fit

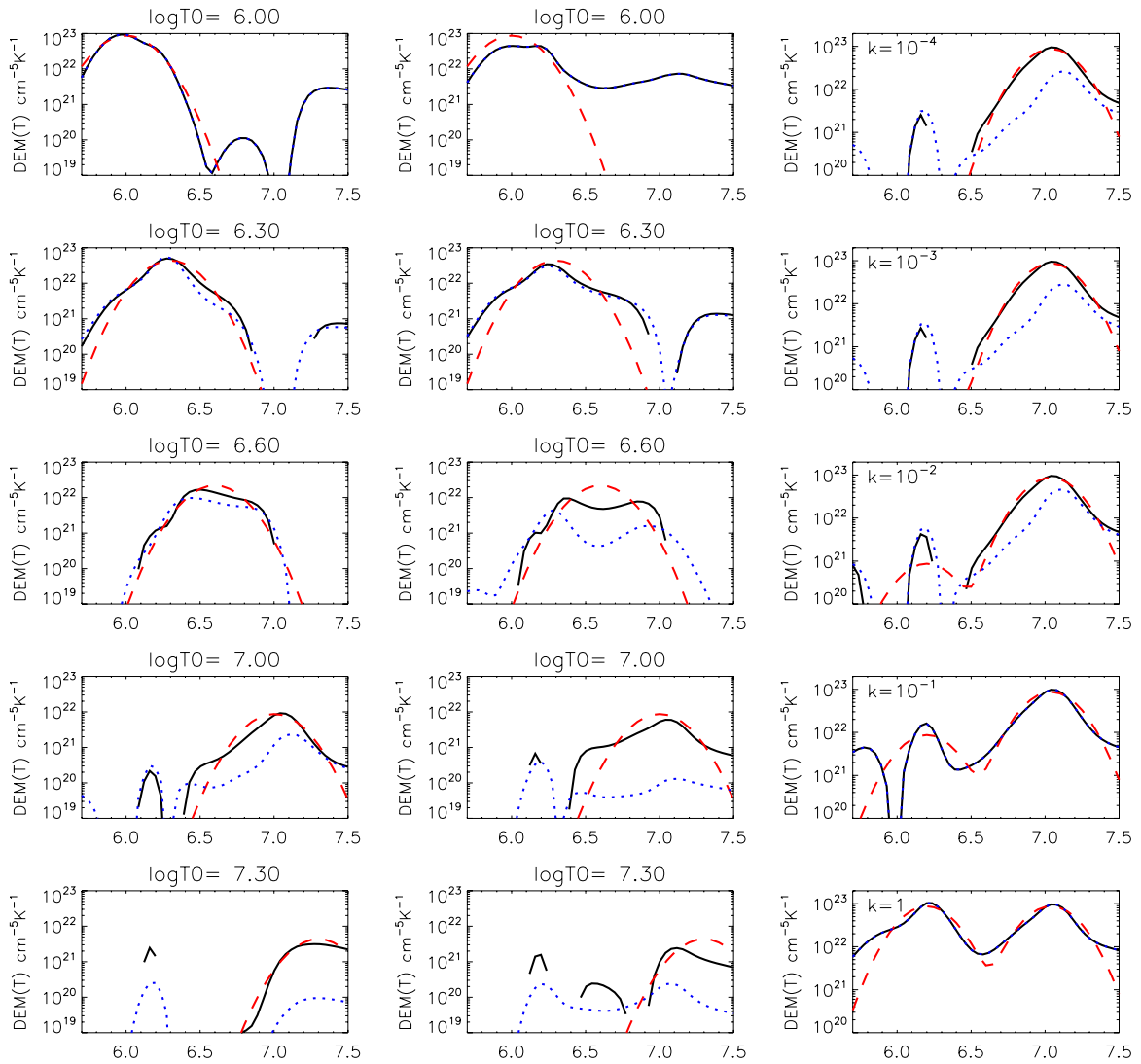


**Figure 5.** Left (top to bottom): idealized Gaussian DEMs for a number of peak temperatures  $\log T_0$  with an assumed error of the AIA data number (DN) of  $\text{DN}_{\text{err}} = \sqrt{\text{DN}}$ . Middle: same as left column but with an included systematic error:  $\text{DN}_{\text{err}} = \sqrt{\text{DN} + (0.2 \times \text{DN})^2}$ . Right: reconstructed DEM from two Gaussian components. The dashed red lines give the input model DEM, the black solid lines are the reconstructed DEM without positivity constraint, and the dotted blue lines are the reconstructed DEM with positivity constraint. The factor  $k$  gives the ratio between the DEM of the cold component and hot component.

(A color version of this figure is available in the online journal.)

of SOL2010-08-14T10:05 suggests a temperature of 10.5 MK, which falls within the main AIA sensitivity range. To investigate the systematics of the DEM code and the influence of parameters such as the data error and use of a positivity constraint in the regularized inversion, we performed a systematic study using idealized Gaussian DEMs with different peak temperatures. From these, the expected AIA data number (DN) was calculated and used to find the DEM from regularized inversion (see the Appendix). In addition, a model with two Gaussian DEMs was used, emulating the often-found double-peak structure of the DEM. Figure 5 shows the model DEM and the reconstructed DEM for several values of peak temperature and several relative intensities in the case of two Gaussians. Generally there is a better agreement between model and reconstructed DEM without the imposed positivity constraint. In the case of purely Poisson error without any systematic terms the shape of the DEM is well reconstructed except for peak temperatures higher than  $\log T \sim 7$ , where some of the DEM seems to be “redistributed” to low temperatures at around  $\log T = 6.2$ . The

same but opposite effect occurs for very low peak temperatures of around  $\log T \sim 6$ . This is probably due to the 193 Å response, which has two peaks, one at  $\log T = 6.2$  and one at  $\log T = 7.2$ . This effect is worsened when the positivity constraint is applied. In all cases, the total emission measure defined as  $\text{EM} = \int_{\log T=5.7}^{\log T=7.5} \xi(T) dT$  is reduced relative to the total model emission measure (Figure 6) by a factor of up to 30 when the positivity constraint is used and up to 2 without the positivity constraint. However, the effect is not systematic enough to allow for implementation of an empirical correction in the DEM reconstruction.

There is also the possibility of several distinct particle populations with different temperatures being present. The mean electron flux spectra derived from AIA at the footpoints and the HXR above-the-looptop source in SOL2012-07-19T05:58 are consistent with a Maxwellian distribution, but with a deviation near 1 keV, while *RHESSI* observes a power-law distribution at energies above 25 keV. Unfortunately, there were no reliable *RHESSI* observations possible between 3 and  $\sim 25$  keV for these

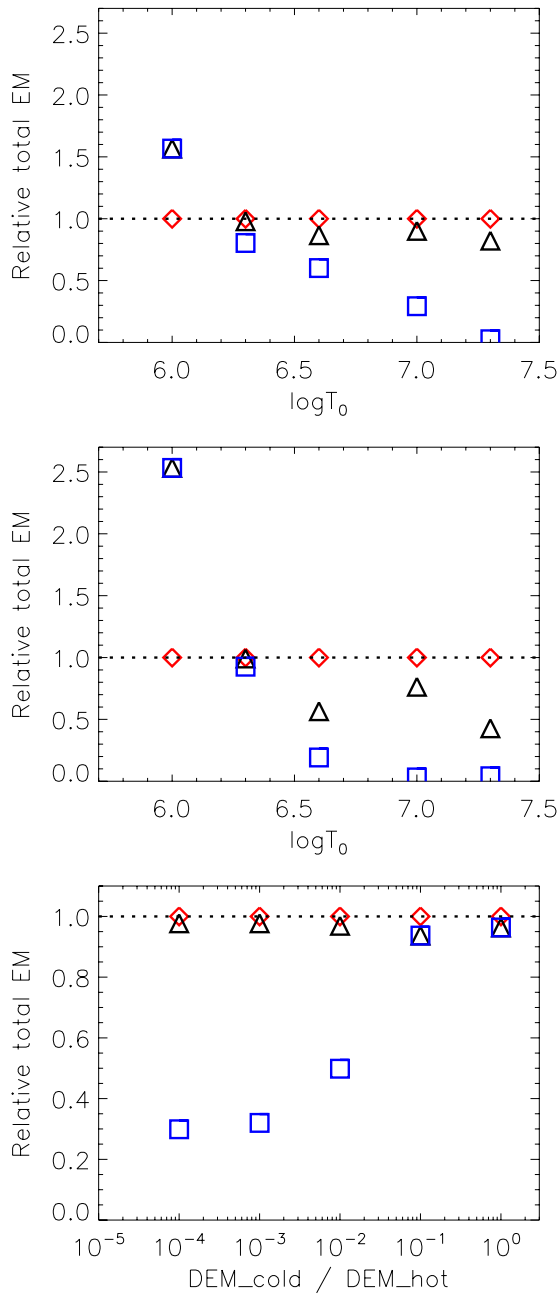


**Figure 6.** Top: total EM relative to total model EM as a function of  $\log T_0$  for data number error of  $\text{DN}_{\text{err}} = \sqrt{\text{DN}}$ . Middle: same as top but with data number error of  $\text{DN}_{\text{err}} = \sqrt{\text{DN} + (0.2 \times \text{DN})^2}$ . Bottom: total EM relative to total model EM in the case of a double-Gaussian model as a function of relative peak emission measure. Red diamonds: model DEM. Black triangles: no positivity constraint. Blue squares: with positivity constraint.

(A color version of this figure is available in the online journal.)

two sources. We fitted a thermal component to the spectrum from imaging spectroscopy of the two sources in this energy range. While potentially not physically meaningful because the spectrum mainly consists of reconstruction noise from the different sources, this provides a reasonable upper limit of the flux (compare Figure 3) and suggests that the presence of a second Maxwellian distribution similar to the one found in the SXR coronal source and in the loop of SOL2010-08-14T10:05 is feasible.

## 5. CONCLUSIONS

Combining X-ray observations with EUV observations from *RHESSI* allows the mean electron flux spectrum from different sources in solar flares to be inferred from 0.1 keV up to several tens of keV, thus enabling diagnostics of the low-energy component of the spectrum inaccessible with *RHESSI* alone. There is still a gap in spectral coverage where uncertainties are rather large at the intermediate energies between about 1 and 3 keV where neither instrument is sensitive for reliable measurements. This is the most likely cause for the discrepancy between the total emission measures of *RHESSI* and AIA. The total spectrum can be described as the combination of a Maxwellian core, a secondary “halo” component, and a non-thermal tail similar to distributions often seen in the solar wind (e.g., Lin et al. 1997). An analytical description of the total solar flare spectrum and a quantitative comparison with solar wind spectra will be the subject of future work.

Financial support by the European Commission through the FP7 HESPE network (FP7-2010-SPACE-263086) is gratefully acknowledged. This work is supported by an STFC Consolidated Grant (E.P.K.) and by the Swiss National Science Foundation (M.B.). We thank the referee for valuable comments and suggestions.

## APPENDIX

### SIMULATED DIFFERENTIAL EMISSION MEASURES

To investigate the influence of parameters such as the data error and use of a positivity constraint in the regularized inversion method that was used for the analysis of the presented events, we performed a systematic study using idealized Gaussian DEMs. An idealized Gaussian DEM in  $\log T$  of the form  $(\text{DEM}_0 / \sqrt{2\pi\sigma}) \exp[-(\log T - \log T_0)^2 / (2\sigma^2)] \times 10^6 / T_0$  was used where  $\sigma = 0.15$  for six values of  $\log T_0$  between 5.8 and 7.5 and  $\text{DEM}_0 = 3.27 \times 10^{22} \text{ cm}^{-5} \text{ K}^{-1}$ . From this, the expected AIA DN was calculated and used to find the DEM from inversion for an assumed data error of  $\text{DN}_{\text{err}} = \sqrt{\text{DN}}$  and including a “systematic error”  $\text{DN}_{\text{err}} = \sqrt{\text{DN} + (0.2 \times \text{DN})^2}$  to account for calibration uncertainties (e.g., Landi & Young 2010). In both cases, the DEM was found once without other constraints and once imposing a constraint for positive DEM at all temperatures. In a second step, a DEM with two Gaussian components (with peak temperatures  $\log T_{\text{cold}} = \log T_{\text{hot}} + k$  with  $k$  between  $10^{-5}$  and 1) was used to emulate the often-observed two-peak structure. Figure 5 shows the input model along with the reconstructed DEMs for all temperatures. We can now define the total emission measure as the integral over the DEM  $\text{EM} = \int_{\log T=5.7}^{\log T=7.5} \xi(T) dT$  and compare this as a function of  $\log T_0$  and  $k$  (Figure 6).

## REFERENCES

- Battaglia, M., & Benz, A. O. 2006, *A&A*, 456, 751  
 Battaglia, M., Grigis, P. C., & Benz, A. O. 2005, *A&A*, 439, 737  
 Battaglia, M., & Kontar, E. P. 2011, *ApJ*, 735, 42  
 Battaglia, M., & Kontar, E. P. 2012, *ApJ*, 760, 142  
 Brown, J. C., & Emslie, A. G. 1988, *ApJ*, 331, 554  
 Emslie, A. G., Kontar, E. P., Krucker, S., & Lin, R. P. 2003, *ApJL*, 595, L107  
 Hannah, I. G., Christe, S., Krucker, S., et al. 2008, *ApJ*, 677, 704  
 Hannah, I. G., & Kontar, E. P. 2012, *A&A*, 539, A146  
 Hannah, I. G., & Kontar, E. P. 2013, *A&A*, 553, A10  
 Holman, G. D., Aschwanden, M. J., Aurass, H., et al. 2011, *SSRv*, 159, 107  
 Hurford, G. J., Schmahl, E. J., Schwartz, R. A., et al. 2002, *SoPh*, 210, 61

- Ireland, J., Tolbert, A. K., Schwartz, R. A., Holman, G. D., & Dennis, B. R. 2013, [ApJ](#), **769**, 89
- Kontar, E. P., Brown, J. C., Emslie, A. G., et al. 2011, *SSRv*, **159**, 301
- Kontar, E. P., Emslie, A. G., Piana, M., Massone, A. M., & Brown, J. C. 2005, *SoPh*, **226**, 317
- Kontar, E. P., Hannah, I. G., Jeffrey, N. L. S., & Battaglia, M. 2010, [ApJ](#), **717**, 250
- Krucker, S., & Battaglia, M. 2013, *ApJ*, submitted
- Krucker, S., Kontar, E. P., Christe, S., Glesener, L., & Lin, R. P. 2011, [ApJ](#), **742**, 82
- Landi, E., & Young, P. R. 2010, [ApJ](#), **714**, 636
- Lemen, J. R., Title, A. M., Akin, D. J., et al. 2012, *SoPh*, **275**, 17
- Lin, R. P., Dennis, B. R., Hurford, G. J., et al. 2002, *SoPh*, **210**, 3
- Lin, R. P., Larson, D. E., Ergun, R. E., et al. 1997, *AdSpR*, **20**, 645
- Liu, W., Chen, Q., & Petrosian, V. 2013, [ApJ](#), **767**, 168
- Marsch, E. 2006, *LRSP*, **3**, 1
- Prato, M., Piana, M., Brown, J. C., et al. 2006, *SoPh*, **237**, 61
- Rossberg, A. G. 2008, *JApS*, **45**, 531
- Simões, P. J. A., & Kontar, E. P. 2013, [A&A](#), **551**, A135
- Smith, D. M., Lin, R. P., Turin, P., et al. 2002, *SoPh*, **210**, 33
- Tandberg-Hanssen, E., & Emslie, A. G. 1988, *The Physics of Solar Flares* (Cambridge: Cambridge Univ. Press)